Check for updates

LASER & PHOTONICS REVIEWS
www.lpr-journal.org

Integrated Microring Spectrometer with In-Hardware Compressed Sensing to Break the Resolution-Bandwidth Limit for General Continuous Spectrum Analysis

Chunlei Sun, Zequn Chen, Yuting Ye, Yang Weng, Kunhao Lei, Hui Ma, Maoliang Wei, Chuyu Zhong, Hongtao Lin, and Lan Li**

Microspectrometers have numerous applications in mobile optical sensing due to their dramatic advantages of compact size, light weight, and low power consumption. Reconstructive spectrometers, based on computational algorithms, have garnered considerable interest as they exhibit superior resolution or spectral bandwidth. However, existing reconstructive spectrometer designs face challenges in spectral applicability, algorithm robustness, and the resolution-bandwidth limit. Here, a reconstructive spectrometer that utilizes a microring resonator (MRR) is proposed to achieve compressed sensing in hardware by decomposing an arbitrary continuous spectrum into a series of simple comb spectra. Owing to the presparse operation of the MRR, one needs to construct the comb spectra with a known line shape, only leaving the amplitude to be solved. Consequent random gratings measure the comb spectra, which are reconstructed with high robustness. Thanks to the independent engineering of spectral resolution and bandwidth, the approach breaks the traditional resolution-bandwidth limit. A narrowband signal of a dual peak at 0.2 nm and a broadband spectrum with a large spectral bandwidth of 60 nm and 300 spectral channels using only eight physical channels is retrieved, achieving an ultrahigh reconstructive compression ratio of 37.5. This work opens up the possibility of on-site spectral spectroscopy applications for the lab-on-a-chip system.

1. Introduction

Spectrometers are cornerstone instruments with applications ranging from fundamental scientific research to industrial process monitoring. With the ever-increasing demand for advanced applications in wearable and Internet-of-Things (IoT) devices for healthcare and food monitoring, the need for integration and miniaturization of spectrometers to realize on-site inspection increases.[1] Future innovative spectrometers need compact, high-resolution, large spectral bandwidth, low power consumption, and compatibility with large-scale manufacturing. Inspired by conventional benchtop spectrometers, a variety of compact, portable spectrometers with reduced footprint and weight have been developed based on the principle of dispersive optics, narrowband filters, and Fourier transforms interferometers.[2–16] Although many efforts have been involved in microspectrometers, using existing on-chip designs is challenging to realize a high-resolution detection over a broad spectral bandwidth for a general unknown spectrum. Moreover, there is an inherent dilemma of balancing power consumption and device footprint.

In the past decade, a new type of spectrometer based on computational spectral reconstruction has emerged,[17–34] since it breaks through the design limitation of conventional spectrometers. Unlike conventional spectrometers based on dispersive

C. Sun, Z. Chen, Y. Ye, Y. Weng, L. Li
Key Laboratory of 3D Micro/Nano Fabrication and Characterization of Zhejiang Province
School of Engineering
Westlake University
Hangzhou 310030, China
E-mail: sunchunlei@westlake.edu.cn; lilan@westlake.edu.cn

C. Sun, Z. Chen, Y. Ye, Y. Weng, L. Li
Institute of Advanced Technology
Westlake Institute for Advanced Study
Hangzhou 310024, China

K. Lei, H. Ma, M. Wei, C. Zhong, H. Lin
Key Laboratory of Micro-Nano Electronics and Smart System of Zhejiang Province
College of Information Science and Electronic Engineering
Zhejiang University
Hangzhou 310027, China

K. Lei, H. Ma, M. Wei, C. Zhong, H. Lin
School of Microelectronics
Zhejiang University
Hangzhou 310027, China

C. Zhong
College of Integrated Circuits and Optoelectronic Chips
Shenzhen Technology University
Shenzhen 518118, China

The ORCID identification number(s) for the author(s) of this article can be found under https://doi.org/10.1002/lpor.202300291

DOI: 10.1002/lpor.202300291

 © 2023 Wiley-VCH GmbH

optics and narrowband filters by spectrum-to-space mapping principle (one frequency mapped to one spatial position), reconstructive spectrometers simultaneously address a full range of spectral components at each detector, which has a robust performance to fabrication imperfections.[19,35] Diverse photonic structures such as random scattering media,[17,18] evanescently coupled multimode spiral,[19,34] and linear coherent integrated networks[20,21] were involved in designing an integrated reconstructive microspectrometer. These structures utilize optical transmission, reflection, scattering, interference, resonance, and absorption effects to distinguish different wavelengths. Strong light–matter interaction in nanophotonic structures can significantly increase the optical path length, making such spectrometers have extreme spectral resolution with a compact size.[36] Developing a measurement matrix consisting of a series of very different, ideally orthogonal, spectral responses is crucial.[35] Thus, the speckle, the different spatial distribution of intensity at the detectors, has a unique mapping relationship with the input spectrum. The spectrum can be reconstructed from the measured speckle pattern usually via compressed sensing (CS) theory and regression algorithm.

CS is a digital signal processing technique that allows fast and efficient reconstruction of a signal by a set of sparse data that is randomly sampled. It requires fewer measurements than the Shannon-Nyquist sampling theorem and has the potential to provide the spectral reconstruction of higher resolution over a broader spectral bandwidth. Therefore, the reconstructive spectrometer is ideally suited for compressed sensing due to the nearly random sampling of its measurement matrix.[37] For a K-sparse unknown spectrum with the dimension N(K <<N), the spectrum can be recovered by finding solutions to an underdetermined linear system via M measurements ($M \geq K$).[37] Typically, the sparsity K is smaller, and the reconstructive compression ratio, expressed as the spectral bandwidth $\Delta\lambda$ divided by the product of the resolution $\delta\lambda$ and M ($\Delta\lambda/(\delta\lambda * M)$), is higher. Therefore, CS is a powerful tool for recovering sparse signals to enhance the spectral bandwidth and resolution using fewer measurements. The key challenge to developing a set of basis functions to make the compressible spectrum signals are well approximated by K-sparse representations. As seen in previous studies,[19,23,28] by just tens of sampling, hundreds of spectral channels can be reconstructed with a compression ratio better than eight. Unfortunately, the CS-based reconstruction algorithm suffers from this dilemma: the input spectrum must be sparse in certain known domains. Otherwise, the recovered spectrum may be damaged for the under-sampling case (M < N). In most practical scenarios, we cannot always find a unified domain to make it sparse since the input spectrum is nonpriori. Thus, the CS-based reconstruction algorithm is difficult to achieve high applicability and robustness, limiting the applications for spectral reconstruction.

In this paper, we proposed an integrated general spectrometer containing a tunable microring resonator (MRR) cascaded with a set of random gratings. CS can be carried out in hardware, in which the MRR makes the spectrum sparse, while the random grating implements random sampling. A set of wavelengths of the incident light satisfying the resonance condition of the tunable MRR will be transmitted to the drop port of the MRR, generating a comb spectrum. The presparse operation makes the unknown input continuous spectrum can be always K-sparse represented to decrease spectrum complexity. Then the sparse spectrum was measured by a few random gratings and reconstructed by the convex optimization method. By applying the heating power (P_i) to the MRR to tune the resonant wavelength across the entire free spectral range (FSR), the retrieved comb spectra at all the tuning states combined into the original input spectrum. Therefore, any complex continuous spectrum can be decomposed into a series of simple comb spectra, making the microspectrometer applicable to the general continuous spectrum. In addition, by optimizing the 3 dB bandwidth and FSR of MRR, and sparsity of comb spectrum, we can break the resolution-bandwidth limit to realize high-resolution and large-bandwidth spectral analysis.

2. Results

2.1. Principle and Design

Figure 1a shows the schematic of the proposed microspectrometer consisting of a thermally tunable MRR, a multistage Y-junction splitter tree, and a series of specially designed random gratings. The spectral analysis process includes four steps: presparse, sampling, reconstruction, and combination, as shown in Figure 1b. The incident broadband spectrum $s(\lambda)$ is coupled into the input waveguide of the MRR and experiences a presparse operation. Only the wavelengths satisfying the resonance condition of the MRR will be transmitted to the drop port of the MRR, forming an almost equally spaced comb spectrum $s_i(\lambda)$ with a series of resonant peaks. By activating the heater via an external heating power (P_i), the resonance position of the MRR will gradually shift. By tuning the resonant wavelength across the entire FSR, the input spectrum $s(\lambda)$ can be recorded by a series of comb spectra, which is mathematically written as

$$s(\lambda) = B(\lambda)\left(\sum_{Q} s_i(\lambda)\right),\ i = 1, 2, \ldots, Q \tag{1}$$

where the letter Q refers to the total tunable states traversing the entire FSR, and the factor $B(\lambda)$ is the wavelength-dependent transmission factor of MRR. The multistage Y-junction splitter tree splits the comb spectrum into multiple channels with equal power. Here, a 1×2 multimode interferometry (MMI) serves as the Y-junction splitter. The random gratings with diverse response spectra sample each comb spectrum at each tuning state, which is finally detected by the photodetectors sequentially after each random grating. The letter j refers to the physical channel number. The measured photocurrent $I_i(j)$ can be expressed as

$$I_i(j) = \int_{\lambda_{\min}}^{\lambda_{\max}} p(\lambda, j)\, s_i(\lambda)\, \mathrm{d}\lambda,\ j = 1, 2, \ldots, M \tag{2}$$

where $\lambda_{\min}$ and $\lambda_{\max}$ are the minimum and maximum wavelength, respectively, and M is the physical channel number or measurement number. $p(\lambda, j)$ is the response function at the channel j from the light source to the photodetectors, in which the fiber-to-chip coupling loss and the spectral responsivity of the photodetectors have been included. $p(\lambda, j)$ can be accurately measured during a precalibration process. In signal processing,

© 2023 Wiley-VCH GmbH

18638899, 0, Downloaded from https://onlinelibrary.wiley.com/doi/10.1002/lpor.202300291 by Westlake University, Wiley Online Library on [23/08/2023]. See the Terms and Conditions (https://onlinelibrary.wiley.com/terms-and-conditions) on Wiley Online Library for rules of use; OA articles are governed by the applicable Creative Commons License

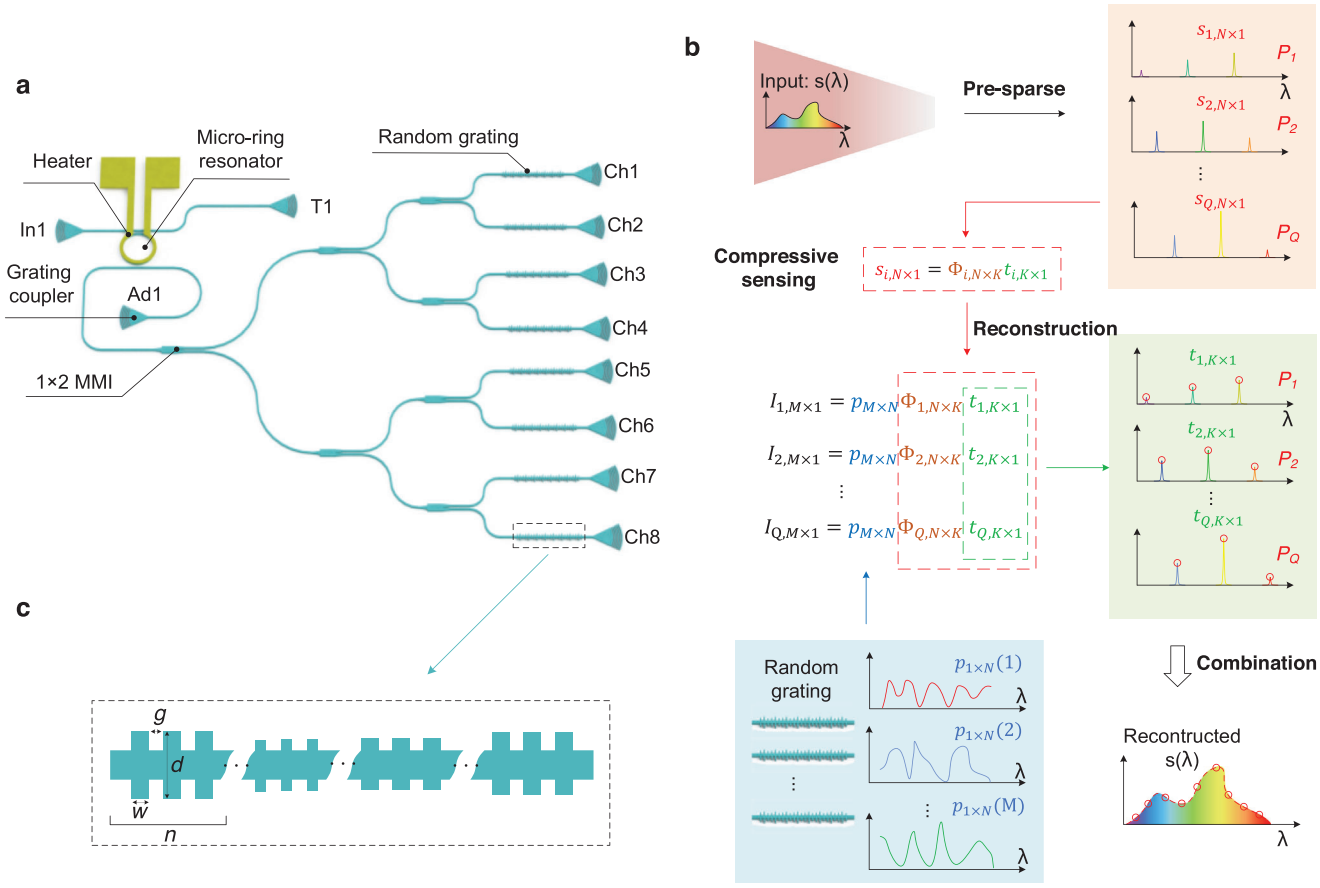

Figure 1. a) Device structure consisting of a tunable MRR, a 1×8 Y-junction tree, and a random grating array. b) Operational principle of the microspectrometer consisting of presparse, sampling, reconstruction, and combination. c) Description of the random grating design with the design parameters to control the spectral response of the random grating.

signal sampling is discrete. Thus Equation (2) can be rewritten in a linear algebra formulation as

$$I_{i,\ M\times1} = p_{M\times N}\ s_{i,\ N\times1} \tag{3}$$

Generally, the physical channel number is much smaller than the dimension of the input spectrum ($M \ll N$). The equation is typically underdetermined with infinite solutions. Although the spectrum only has a few nonzero coefficients, the inversion and standard linear regression methods (LRM) are inefficient in solving the underdetermined problem due to the measurement error and noise. Many regularization techniques and constrained optimization methods, such as non-negative least squares,[38] Tikhonov regularization,[28,29] and sparse recovery-based algorithms,[38,39] have been used to overcome the limitations and solve the underdetermined problem. However, a high-compression-ratio and robust spectrum reconstruction are difficult to achieve since many parameters, such as bandwidth, amplitude, and the locations of nonzero coefficients, need to be solved. Considering the spectrum after the MRR is naturally sparse, each peak will be approximately ideal Lorentzian-shaped if there is no backward propagating mode in the MRR with excellent sidewall smoothness.[40] Each resonant peak in the wavelength constitutes the orthonormal Lorentz function basis. Hence, the comb spectrum is K-sparse in the Lorentz basis space. The CS method can be utilized to enhance the spectrum reconstruction. Since the central wavelength and bandwidth of each peak can be obtained by precalibration, only the amplitude of peaks needs to be solved. The comb spectrum can be represented as a linear combination of Lorentz functions

$$s_{i,\ N\times1} = \Phi_{i,\ N\times K}\ t_{i,\ K\times1} \tag{4}$$

where $t_{i,\ K\times1}$ is the $K\times1$ column vector of weighting coefficients. $\Phi_{i,\ N\times K}$ is the basis matrix whose columns are all Lorentz functions, which can be obtained by precalibration. By substituting Equation (4) into Equation (3), $I_{i,\ M\times1}$ can be written as

$$I_{i,\ M\times1} = \Theta_{i,M\times K}\ t_{i,\ K\times1} \tag{5}$$

where $\Theta_{i,M\times K} = p_{M\times N}\ \Phi_{i,\ N\times K}$. By the presparse operation and the CS method, the dimension of the unknown signal to be solved is compressed from N to K. The problem may appear well-conditioned, provided that $M \geq K$. The $t_{i,\ K\times1}$ can be obtained by solving Equation (5) using the convex optimization method

$$\text{Minimize } \left|\left|I_i - \Theta_i \cdot t_i\right|\right|_2^2 + \alpha \left|\left|t_i\right|\right|_2^2 \text{ subject to } 0 \leq t_i \leq 1 \tag{6}$$

© 2023 Wiley-VCH GmbH

18638899, 0, Downloaded from https://onlinelibrary.wiley.com/doi/10.1002/lpor.202300291 by Westlake University, Wiley Online Library on [23/08/2023]. See the Terms and Conditions (https://onlinelibrary.wiley.com/terms-and-conditions) on Wiley Online Library for rules of use; OA articles are governed by the applicable Creative Commons License

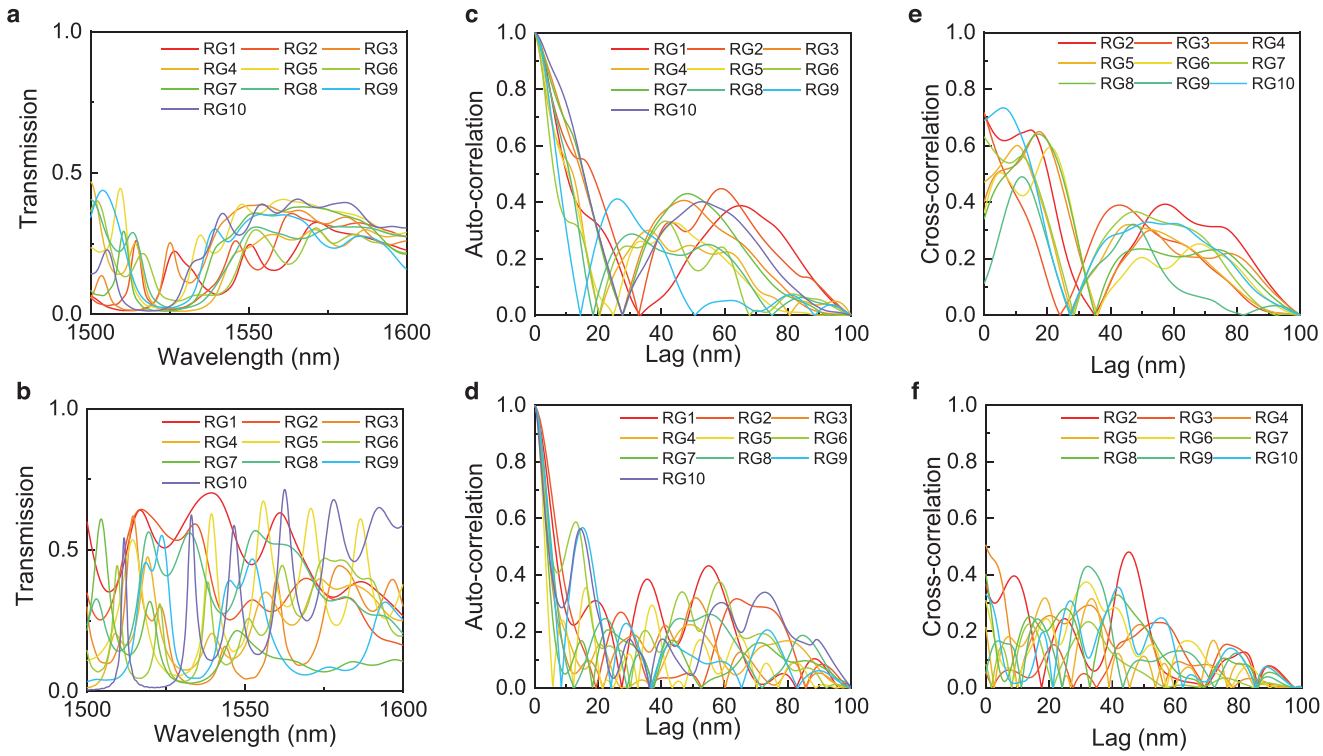

Figure 2. Simulated transmission spectra of ten a) CDGFs and b) PDGFs. Autocorrelation of the response spectra of the ten c) CDGFs and d) PDGFs. The wavelength lag between the response spectra refers to a translation operation mathematically. Crosscorrelation between the first grating and the other gratings for e) CDGFs and f) PDGFs. The legend RG1 refers to the first random grating.

where the weight coefficient α is estimated from a crossvalidation analysis.[41] Thus, the comb spectrum s_i at each tunable state can be attained by Equation (4). Finally, the original input spectrum is recovered by combining all the retrieved comb spectra by Equation (1).

Obviously, it can retrieve the comb spectrum simply by using more random gratings or physical channels. However, fewer channels keep a small footprint and a high signal-noise ratio of the spectrometer. It is possible to recover K-sparse spectra using almost as many channels ($M \approx K$) if the rank of $\Theta_{i,M\times K}$ is as large enough.[37] Usually, the matrix $p_{M\times N}$ is incoherent with $\Phi_{i,\ N\times K}$. Therefore, the rank of matrix $p_{M\times N}$ needs to be as large as possible, in other words, the rows of $p_{M\times N}$ $[p_{1\times N}(1),\ p_{1\times N}(2), \ldots, p_{1\times N}(M)]$ have to be orthogonal. Intuitively, the key to achieving a response matrix $p_{M\times N}$ with a high rank is to make random gratings very different. A crosscorrelation function can characterize the similarity between each pair of the random grating response spectra at different wavelengths. A value smaller than 0.5 indicates a moderate or weak correlation between different random gratings. The minimum distinguished wavelength interval can be estimated by the full-width half maximum (FWHM) of the autocorrelation of the random grating response spectra,[19] which illustrates fast and random features. It is difficult to achieve a response matrix $p_{M\times N}$ with small autocorrelation and crosscorrelation simultaneously. In addition to presparse operation, the MRR can achieve high resolution due to its deep sub-nanometer bandwidth. Thus, the design of the random gratings is relieved, and the FWHM of the autocorrelation only needs to be smaller than the FSR of the MRR. Therefore, the resolution is dramatically boosted by the MRR while maintaining a large spectral bandwidth.

These desired response spectra of random gratings are achieved by introducing randomness in the constraint parameters space, as shown in Figure 1c. Compared to the completely disordered grating filters (CDGFs) in which each pitch is different, our proposed partially disordered grating filters (PDGFs) consist of multiple subgroups. Each subgroup consists of a small number of repeated pitches to increase the selectivity of the spectrum without apparent loss. The PDGFs mainly work in the Bragg reflection region rather than subwavelength or radiation regions, which makes the spectra vary fast, and decrease transmission loss. To clarify the advantage of our proposed PDGFs, a full comparison between CDGFs and PDGFs is given in **Figure 2**. For the devices working around 1550 nm, the parameters w and g vary between 190 and 240 nm, while d varies between 350 and 500 nm. Both the CDGF and PDGF contain a total of about 60 pitches. The design parameters w, g, and d are random integers with a step of 2 nm. For the CDGFs, n is equal to 1, while n is a random even number ranging from 2 to 8 for the PDGFs. The letter n refers to the number of repeated pitches in a subgroup of the partially disordered gratings. The detailed structural parameters of PDGFs are given in Note S1 in the Supporting Information. The response spectra of the ten CDGFs and ten PDGFs are shown in Figure 2a,b, respectively. The PDGFs have faster, more random, and lower loss response spectra than those of the CDGFs. Figure 2c,d demonstrate the autocorrelation of the response

© 2023 Wiley-VCH GmbH

18638899, 0, Downloaded from https://onlinelibrary.wiley.com/doi/10.1002/lpor.202300291 by Westlake University, Wiley Online Library on [23/08/2023]. See the Terms and Conditions (https://onlinelibrary.wiley.com/terms-and-conditions) on Wiley Online Library for rules of use; OA articles are governed by the applicable Creative Commons License

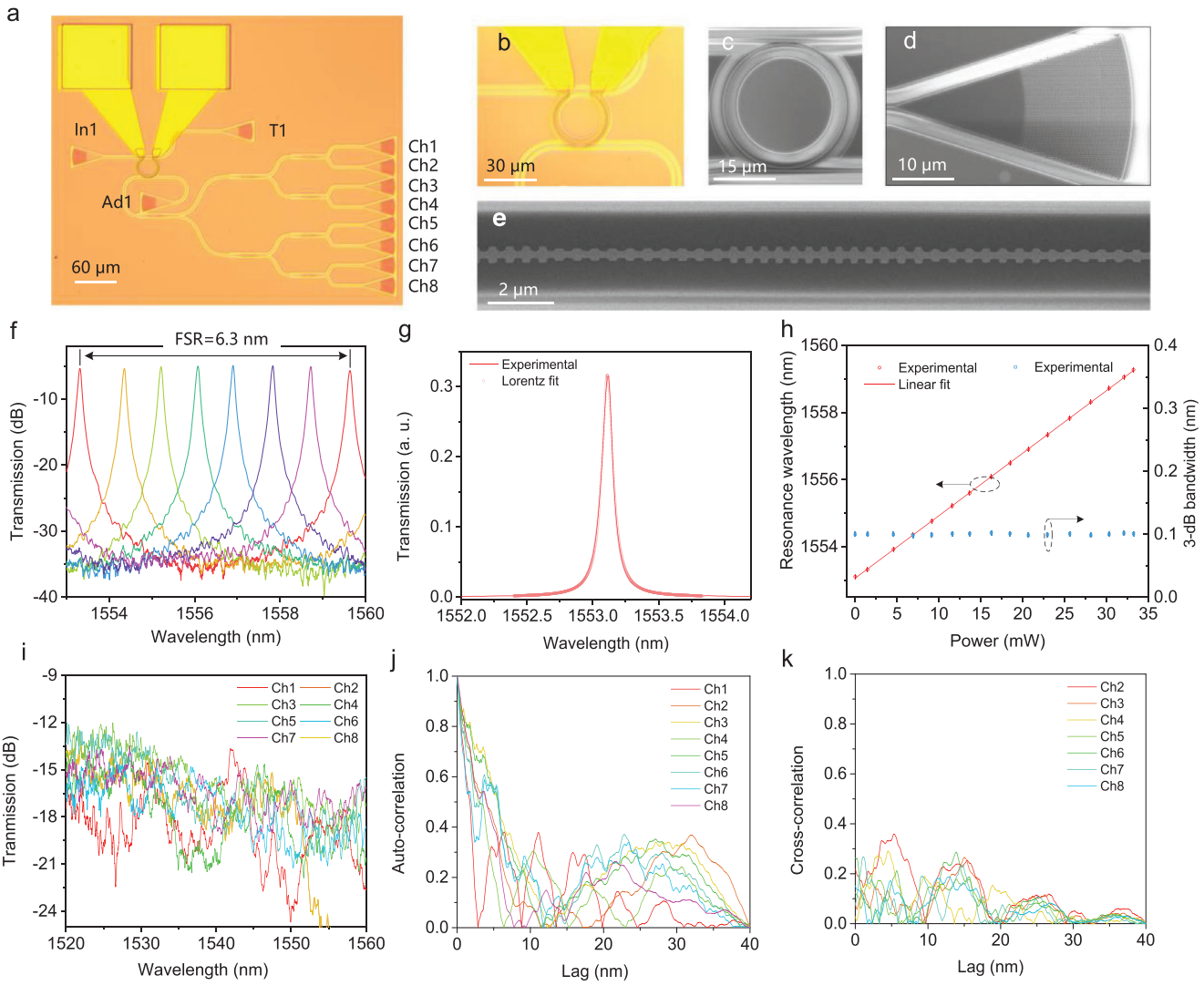

Figure 3. a) Microscope image of the entire microspectrometer. b) Zoom-in view of the tunable MRR. SEM images of c) MRR, d) grating coupler, and e) random grating. f) Transmission spectra of the MRR with different driving power. g) Lorentz fit of the resonant peak of the MRR. h) Resonant wavelength (red circle) and 3 dB bandwidth (blue square) of the resonant peak versus the driving power. The solid red curve shows the linear fit of resonant wavelength versus the driving power. The error bars indicate standard deviations of resonant wavelength and 3 dB bandwidth. i) Normalized response matrix $p_{M\times N}$. j) Autocorrelation of the measured spectrum of a single channel. k) Crosscorrelation between the measured spectrum spectra of the first channel and other channels.

spectra of the CDGFs and PDGFs, respectively. The FWHM of autocorrelation of the CDGFs is about 10–20 nm, while the FWHM of PDGFs is smaller than 10 nm. This autocorrelation provides an estimate of the spectral resolution of the random gratings. We calculated the crosscorrelation between the first grating and the other gratings for the CDGFs and PDGFs. For the CDGFs, the crosscorrelation is higher than 0.5 in Figure 2e, verifying the similarity of the response spectra. While for the PDGFs, the crosscorrelation in the entire working band is lower than 0.5, as shown in Figure 2f. On the other hand, we also utilized the singular value decomposition to valuate the matrix orthogonality of the response matrix of CDGFs and PDGFs, which has been widely applied in solving ill-posed inverse problems.[34,42,43] The SV curve of our proposed PDGFs is smoother and has a slower decay than that of CDGFs, and the kink is not clearly visible (Note S1, Supporting Information), which agrees well with the results in Figure 2. Therefore, we can achieve high-performance random filters with fast and different response spectra by adopting PDGFs.

2.2. Device Characterization

Figure 3a shows the microscope image of the microspectrometer based on the eight-channel random filter array with a footprint of 310 μm×215 μm. "In1", "T1" and "Ad1" represent the input, through, and add ports of the MRR. The zoom-in image of the tunable MRR is exhibited in Figure 3b. Figure 3c–e shows the

© 2023 Wiley-VCH GmbH

18638899, 0, Downloaded from https://onlinelibrary.wiley.com/doi/10.1002/lpor.202300291 by Westlake University, Wiley Online Library on [23/08/2023]. See the Terms and Conditions (https://onlinelibrary.wiley.com/terms-and-conditions) on Wiley Online Library for rules of use; OA articles are governed by the applicable Creative Commons License

scanning electron microscope (SEM) images of the MRR, grating coupler, and random filter. Before performing the spectrum reconstruction, $\Theta_{i,M\times K}$ and $p_{M\times N}$ need to be precalibrated. The experimental setup for precalibration is illustrated in Note S1 in the Supporting Information. To overcome the influence of the undesired environment temperature (about 21 °C) variation, we characterized the device with a fixed temperature of 25 °C using a commercial thermoelectric cooler. The experimental comb spectra of the MRR from Ad1 to T1 port are shown in Figure 3f. To attain a moderate FSR, the designed radius of MRR is 15 μm, and the coupling gaps at the In1 and Ad1 ports are 200 nm. The FSR of the MRR was measured to be about 6.3 nm at the wavelength of 1553.11 nm. For fitting a resonant peak of MRR, the Lorentz function is a preferred model, achieving a high *R*-Square of 0.999, as shown in Figure 3g. The 3 dB bandwidth of the MRR is fitted to be 0.1 nm at 1553.11 nm. The applied heating power on the heater was increased from 0 to 33.23 mW. The resonant wavelengths are almost perfectly linearly with the heating power, as shown in Figure 3h. The *R*-square coefficient of the linear regression fitting method, which determines the fitting degree, is >0.99995. The tuning efficiency is 0.186 nm mW^{-1}. Thus, the basis matrix $\Theta_{i,M\times K}$ at the *i*th tuning state can be obtained by the Lorentz function of the resonant peaks. Thanks to the almost perfect fitting, the comb spectra can be presented with a low error by the linear combinations of the Lorentz functions. The extinction ratio of the MRR is about 29 dB in the range of 1520–1560 nm.

Figure 3i shows the measured response matrix $p_{M\times N}$ with a wavelength sampling interval of 0.01 nm. The response matrix $p_{M\times N}$ is normalized by subtracting the loss of grating couplers. The insertion loss of each channel is about 12–14.5 dB. Considering the intrinsic loss of the three-level Y-junction tree as the power splitter is 9 dB, the excess loss is 3–5.5 dB, which can be mainly attributed to the scattering loss of cascaded 1 × 2 MMIs and random gratings. The precalibration process of $p_{M\times N}$ is shown in Note S1 in the Supporting Information. The power imbalance of the eight channels, defined by the difference in maximum transmittance of each channel, is smaller than 3 dB. The power imbalance plays an important role in the reconstruction error. Generally, the power imbalance is larger, and the reconstruction error is higher.[28] Figure 3j demonstrates the autocorrelation of the response spectra of the eight physical channels. The formula of the correlation function is given in ref. . The FWHM of autocorrelation is <6 nm, which is smaller than the FSR but much larger than the 3 dB bandwidth of the MRR. We also calculate the crosscorrelation between the first grating and the other gratings. The crosscorrelation in the entire working band is lower than 0.4, as shown in Figure 3k.

To test the performance of the fabricated microspectrometer, we first constructed the comb spectra. By using the signal processing procedure described in Equations (3)−(6), the comb spectra for heating power of 0 mW and 18.49 mW were reconstructed. To evaluate the accuracy of the reconstruction, the relative reconstruction error can be calculated as follows

$$\varepsilon = \frac{\left[\sum_{i=1}^{N}\left(S-S_0\right)^2\right]^{1/2}}{\left(\sum_{i=1}^{N} {S_0}^2\right)^{1/2}} \tag{7}$$

where S denotes the reconstructed spectrum, S_0 is the original spectrum, and N represents the total number of wavelength channels. The normalized retrieved and reference comb spectra with a sparsity of $K = 6$ are shown in **Figure 4**a,b, which are in good agreement with each other.

The precalibrated response matrix $p_{M\times N}$ and comb spectra at all the tuning states were used for spectrum reconstruction. We utilized an amplified spontaneous emission (ASE) source combining one or two tunable filters (WLPhotonics) to obtain the single-peak or dual-peak spectra. The dual-peak spectrum exhibited a 3 dB bandwidth of 0.15 nm and a separation of 0.2 nm. The edges of the single-peak and dual-peak spectra reached as high as 90 dB nm^{-1}. The reconstructed and original spectra are depicted in Figure 4c,d, respectively. A broadening phenomenon can be observed, which can be attributed to the fact that the bandwidth and spacing of the single/dual peaks are comparable to the 3 dB bandwidth of MRR, approaching the resolution limit. Additionally, with the tunable filter possessing very sharp edges, its highest frequency component extended significantly beyond the 3 dB bandwidth of MRR.[44] An MRR with a narrower 3 dB bandwidth can effectively weaken the broadening phenomenon. Next, we test the capability to reconstruct broadband spectra. A spectrum containing a narrow, deep dip with an extinction ratio of 30 dB on a smooth broadband background was retrieved, as shown in Figure 4e. We also used a commercial arrayed waveguide grating to generate a Gaussian-like spectrum as the input signal. The experimental setup for spectra construction is illustrated in Note S1 in the Supporting Information. All the detected input comb spectra were retrieved and are then combined to produce the original input spectrum. The retrieved spectrum and input broadband source are shown in Figure 4f. The total sampling time and energy consumed by MRR for Q scans are 0.63 s and 20.9 mJ for a scan speed of 400 Hz, which can be reduced to 25.2 ms and 0.84 mJ when the scan speed increases to 10 kHz. The calculations are presented in Note S5 in the Supporting Information.

3. Discussions

Improving spectral channels defined as the quotient of spectral bandwidth and resolution is a perpetual pursuit for microspectrometers. It needs to optimize the resolution and bandwidth, as shown by the strategies in **Figure 5**. The utilization of an MRR with a higher quality factor can enhance spectral resolution to a level of a picometer without diminishing the FSR.[43,45] To increase the spectral bandwidth, the most straightforward method is to employ an MRR with a larger FSR. In this regard, we have used an MRR with a 9.4 μm radius to increase the FSR to 10.13 nm, which led to a spectral bandwidth of about 60 nm (Supplementary Note 2). The received optical power is not significantly reduced, as the sparsity and physical channel number remain unchanged. By implementing thermal isolation trenches around the MRR,[14] the tuning range can be expanded up to 30 nm with low power consumption. Another method is to analyze the comb spectrum with more peaks at once. However, there is a trade-off between the number of peaks and the reconstruction error, and the reconstruction error also increases with the increased sparsity of the comb spectrum (Note S3, Supporting Information). When the crosscorrelation of the response spectrum

© 2023 Wiley-VCH GmbH

18638899, 0, Downloaded from https://onlinelibrary.wiley.com/doi/10.1002/lpor.202300291 by Westlake University, Wiley Online Library on [23/08/2023]. See the Terms and Conditions (https://onlinelibrary.wiley.com/terms-and-conditions) on Wiley Online Library for rules of use; OA articles are governed by the applicable Creative Commons License

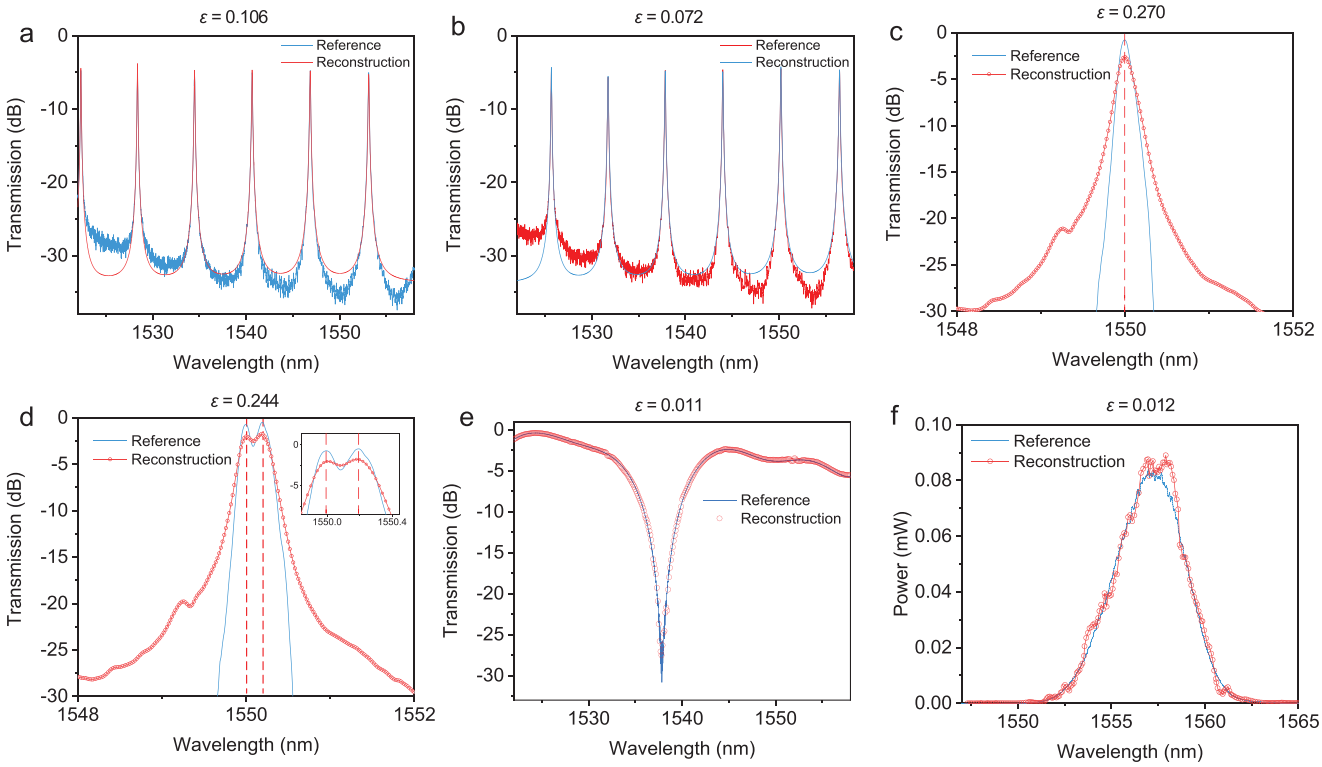

Figure 4. Reconstructed (red line) and reference (blue line) comb spectrum with a sparsity of 6. The comb spectrum is generated from a broadband spectrum input into the MRR with a driving power of a) 0 mW and b) 18.49 mW. c–e) Retrieved spectrum (red) for input spectra (blue) at different conditions. The red points are the reconstructed data using the experimental response matrix $p_{M\times N}$ and comb spectra at each tuning state. c) Reconstructed spectra using the spectrum with single narrowband peak input with 3 dB bandwidth of 0.15 nm. d) Reconstructed spectra using the spectrum with two narrowband peaks input with a 3 dB bandwidth of 0.15 nm and a resonant wavelength interval of 0.2 nm. Inset shows the enlarged figure near the dual peak. e) Reconstructed spectra using the broadband spectrum with a deep dip. f) Retrieved spectrum (red) for an experimentally generated Gaussian-like spectrum (blue) using a commercial arrayed waveguide grating.

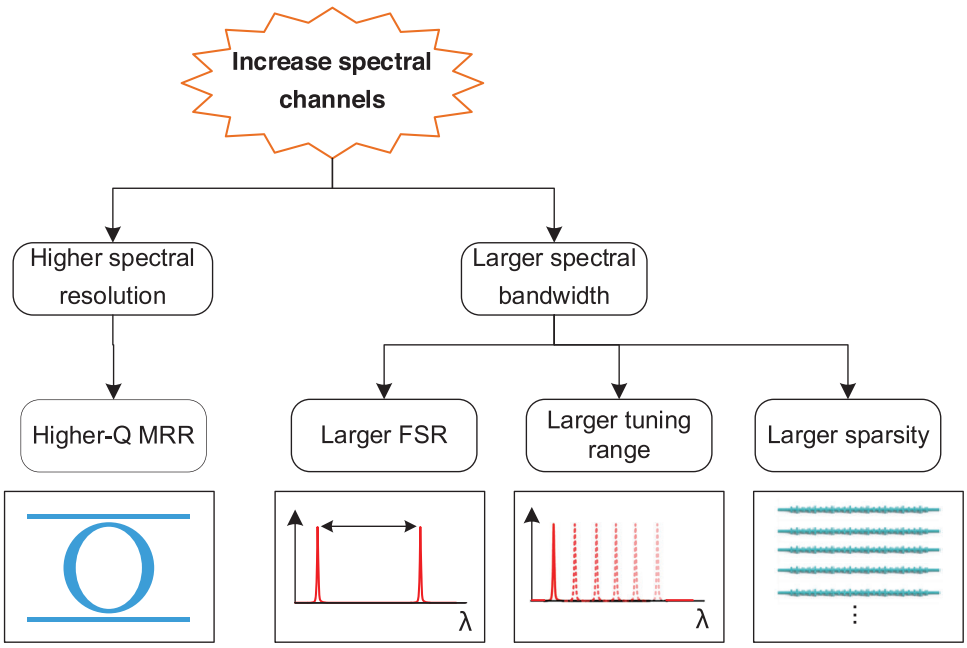

Figure 5. The optimization strategies to increase the spectral channels.

© 2023 Wiley-VCH GmbH

18638899, 0, Downloaded from https://onlinelibrary.wiley.com/doi/10.1002/lpor.202300291 by Westlake University, Wiley Online Library on [23/08/2023]. See the Terms and Conditions (https://onlinelibrary.wiley.com/terms-and-conditions) on Wiley Online Library for rules of use; OA articles are governed by the applicable Creative Commons License

Table 1. Comparison of the reported integrated reconstructive spectrometers.

Spectrometer	Spectral resolution	Spectral bandwidth	Spectral channels	Physical channels	Reconstructive compression ratio	Passive or active	Footprint	Applicability of spectral analysis
Disordered photonic chip[17]	0.75 nm	25 nm	33	25	1.3	Passive	50×25 μm^2	Sparse
Disordered photonic chip[18]	0.25 nm	30 nm	120	8	15	Passive	30×12.8 μm^2	Sparse
Multimode spiral waveguide[19]	0.01 nm	2 nm	200	40	5	Passive	500×500 μm^2	Sparse
Coherent network[20]	0.02 nm	12 nm	600	64	9.4	Passive	520×220 μm^2	Sparse
Stratified waveguide filters[28]	0.45 nm	180 nm	400	32	12.5	Passive	35×260 μm^2	Sparse
Cascaded nanobeam cavities[29]	0.32 nm	16 nm	50	3	16.7	Active	18×250 μm^2	Sparse
Cascaded MRR[31]	0.17 nm	12 nm	70	3	23	Passive	–	Sparse
Dual MRR[32]	0.04	100	2501	1	2501	Active	60×60 μm^2	Sparse
2D disordered microring lattice[33]	0.015 nm	40 nm	2667	4096	0.65	Passive	1000×1000 μm^2	–
Multimode spiral Waveguide[34]	0.016 nm	2 nm	125	12	10.4	Active	1600×2100 μm^2	Sparse
MRR + random gratings (this work)	0.2 nm	60 nm	300	8	37.5	Active	310×215 μm^2	General

of the random grating is nearly orthogonal, the sparsity limit approaches the number of random gratings *M*. It can always attain a larger spectral bandwidth consisting of more resonant peaks by simply using more random gratings, which does not increase the reconstruction error (Figure S4d in Note S3, Supporting Information). Therefore, to effectively increase spectral channels, we can independently enhance the spectral resolution (using a higher quality-factor MRR) and the spectral bandwidth (via a larger FSR, tuning range, and sparsity).

Table 1 highlights state-of-the-art integrated reconstructive spectrometers. The previously reported schemes can tackle a lot of spectral channels. However, the spectrum must be sparse in the known domain, and the sparsity should be smaller than the physical channel number. A complex spectrum requires a complex reconstruction model such as multifeature reconstruction via a modified regularization method with more weight coefficients and more computation power.[28,32] Moreover, the reconstructive error of reconstructive spectrometers increases as the spectrum's complexity. Therefore, it is desired for the reconstructive spectrometers to recover particular and simple spectra by CS method in software. Otherwise, the number of physical channels required would be significantly greater than the number of spectral channels, increasing system complexity and power consumption.[33] Our scheme utilizes the MRR to achieve CS in hardware by decomposing any complex continuous spectrum into a series of simple comb spectra. By precalibration of the MRR and response matrix, the general input continuous spectrum can be successfully retrieved. The proposed spectrometer offers a remarkable combination of high resolution and large spectral bandwidth, achieved with only a few physical channels and a compact design suitable for general spectrum analysis. Thus, a high spectral reconstructive compression ratio of 37.5, defined as the quotient of spectral channels and physical channels, is achieved. Detailed comparison between the conventional and our proposed reconstructive spectrometer is given in Note S4 in the Supporting Information. The spectral resolution is determined by the 3 dB bandwidth of the MRR. Compared to the previously reported MRR-based spectrum system whose spectral bandwidth is limited by the FSR,[31] the spectral bandwidth of our proposed scheme depends on both the sparsity of the comb spectrum and the FSR of the MRR (about *K**FSR). Despite the existence of MRR-based spectrometers that can overcome the limitation of FSR, such solutions often necessitate either significant power consumption or quite a fine wavelength tuning.[14,32] Integrating a single spectrometer with a reconfigurable optical network can effectively enhance spectral bandwidth, but the control of such a network is complex and significantly increases the power consumption and size of the system.[34] Notably, in our scheme, the spectral resolution and bandwidth can be independently engineered, breaking the traditional resolution-bandwidth limit with low power consumption and small spatial occupation.

4. Conclusion

In conclusion, an integrated microspectrometer, including a tunable MRR and a set of random gratings, was experimentally demonstrated. Owing to the presparse operation of MRR, one only needs to reconstruct the sparse comb spectra. By precalibration of the resonant wavelengths and 3 dB bandwidth, the unknown parameter space to be solved is reduced to the amplitude of each resonant peak. Any complex continuous spectrum can be decomposed into a series of simple comb spectra and consequently, be retrieved and combined. Therefore, this is a general spectrometer powerful for various nonpriori continuous spectra. We experimentally achieved a high resolution of 0.15 nm for a single peak and 0.2 nm for a dual peak, and a large spectral bandwidth of 60 nm. In addition, the resolution and spectral bandwidth can be independently engineered, allowing for unprecedented control and breaking the traditional resolution-bandwidth limit. Such microspectrometers may open up pathways toward on-site spectral analytical applications such as on-chip chemical and biological sensing and food monitoring.

© 2023 Wiley-VCH GmbH

18638899, 0, Downloaded from https://onlinelibrary.wiley.com/doi/10.1002/lpor.202300291 by Westlake University, Wiley Online Library on [23/08/2023]. See the Terms and Conditions (https://onlinelibrary.wiley.com/terms-and-conditions) on Wiley Online Library for rules of use; OA articles are governed by the applicable Creative Commons License

5. Experimental Section

The microspectrometer was fabricated on a 220 nm silicon-on-insulator platform with the processes of electron beam lithography (Raith Voyager) and subsequent inductively coupled plasma (Samco). The waveguides and grating couplers were formed by fully etching with a depth of 220 nm. Then a 600 nm thick silica film was then deposited by plasma-enhanced chemical vapor deposition (PECVD) process, covering the whole device. Titanium, chromium, and gold with different thickness combinations were patterned by an ultraviolet lithography process and were deposited by the E-beam evaporator process to realize the thermo-optical heater (100 nm Ti/ 10 nm Au) and contact pads (5 nm Cr/100 nm Au). The width of the titanium heater was 2.75 µm. Meanwhile, a 250 nm thick layer of SiN was deposited by PECVD over the device to prevent the titanium heater from further oxidization. Contact pad windows were opened for electrical probes to connect with circuits for microheater driving.

Supporting Information

Supporting Information is available from the Wiley Online Library or from the author.

Acknowledgements

C.S. and Z.C. contributed equally to this work. The authors would like to acknowledge the Westlake Center for Micro/Nano Fabrication and Instrumentation, the Service Center for Physical Sciences (Zhen Yang's assistance in SEM characterization) at Westlake University, and the ZJU Micro-Nano Fabrication Center at Zhejiang University for the facility support. The authors would also like to thank Xue Wang, Qing Zhao, Yating Pan, and Ting Chen for their help in device fabrication. This article was funded by the National Natural Science Foundation of China (62205274, 62175202, 12104375, 61975179, and 91950204); the National Key Research and Development Program of China (2019YFB2203003); the Zhejiang Provincial Natural Science Foundation of China (LD22F040002); and the Leading Innovative and Entrepreneur Team Introduction Program of Zhejiang (2020R01005).

Conflict of Interest

The authors declare no conflict of interest.

Data Availability Statement

The data that support the findings of this study are available from the corresponding author upon reasonable request.

Keywords

integrated optics devices, optical filters, spectrometers

Received: April 1, 2023
Revised: July 10, 2023
Published online:

[1] Z. Yang, T. Albrow-Owen, W. Cai, T. Hasan, *Science* **2021**, *371*, eabe0722.
[2] G. Calafiore, A. Koshelev, S. Dhuey, A. Goltsov, P. Sasorov, S. Babin, V. Yankov, S. Cabrini, C. Peroz, *Light: Sci. Appl.* **2014**, *3*, e203.
[3] Z. Zhang, Y. Wang, J. Wang, D. Yi, D. W. U. Chan, W. Yuan, H. K. Tsang, *Photonics Res.* **2022**, *10*, A74.
[4] Z. Zhang, Y. Wang, H. K. Tsang, *ACS Photonics* **2021**, *8*, 1251.
[5] Z. Xia, A. A. Eftekhar, M. Soltani, B. Momeni, Q. Li, M. Chamanzar, S. Yegnanarayanan, A. Adibi, *Opt. Express* **2011**, *19*, 12356.
[6] S. Zheng, H. Cai, J. Song, J. Zou, P. Y. Liu, Z. Lin, D.-L. Kwong, A.-Q. Liu, *IEEE Photonics J.* **2019**, *11*, 6602809.
[7] D. Pohl, M. Reig Escalé, M. Madi, F. Kaufmann, P. Brotzer, A. Sergeyev, B. Guldimann, P. Giaccari, E. Alberti, U. Meier, R. Grange, *Nat. Photonics* **2020**, *14*, 24.
[8] M. C. Souza, A. Grieco, N. C. Frateschi, Y. Fainman, *Nat. Commun.* **2018**, *9*, 665.
[9] D. M. Kita, B. Miranda, D. Favela, D. Bono, J. Michon, H. Lin, T. Gu, J. Hu, *Nat. Commun.* **2018**, *9*, 4405.
[10] L. Zhang, J. Chen, C. Ma, W. Li, Z. Qi, N. Xue, *Laser Photonics Rev.* **2021**, *15*, 2100016.
[11] Y. M. Sabry, D. Khalil, T. Bourouina, *Laser Photonics Rev.* **2015**, *9*, 1.
[12] A. Li, J. Davis, A. Grieco, N. Alshamrani, Y. Fainman, *Photonics Res.* **2020**, *8*, 219.
[13] A. Herrero-Bermello, J. Li, M. Khazaei, Y. Grinberg, A. V. Velasco, M. Vachon, P. Cheben, L. Stankovic, V. Stankovic, D.-X. Xu, J. H. Schmid, C. Alonso-Ramos, *Opt. Lett.* **2019**, *44*, 5840.
[14] S. N. Zheng, J. Zou, H. Cai, J. F. Song, L. K. Chin, P. Y. Liu, Z. P. Lin, D. L. Kwong, A. Q. Liu, *Nat. Commun.* **2019**, *10*, 2349.
[15] C. Sun, Z. Chen, Y. Yin, Y. Ye, Y. Luo, H. Ma, J. Jian, Y. Shi, C. Zhong, D. Zhang, H. Lin, L. Li, *ACS Photonics* **2022**, *9*, 2973.
[16] C. Sun, Y. Yin, Z. Chen, Y. Ye, Y. Luo, H. Ma, L. Wang, M. Wei, J. Jian, R. Tang, H. Dai, J. Wu, J. Li, D. Zhang, H. Lin, L. Li, *PhotoniX* **2022**, *3*, 12.
[17] B. Redding, S. F. Liew, R. Sarma, H. Cao, *Nat. Photonics* **2013**, *7*, 746.
[18] W. Hadibrata, H. Noh, H. Wei, S. Krishnaswamy, K. Aydin, *Laser Photonics Rev.* **2021**, *15*, 2000556.
[19] B. Redding, S. Fatt Liew, Y. Bromberg, R. Sarma, H. Cao, *Optica* **2016**, *3*, 956.
[20] Z. Zhang, Y. Li, Y. Wang, Z. Yu, X. Sun, H. K. Tsang, *Laser Photonics Rev.* **2021**, *15*, 2100039.
[21] Y. Li, Z. Zhang, Y. Wang, Y. Yu, X. Zhou, H. K. Tsang, X. Sun, *ACS Photonics* **2023**, *10*, 1012.
[22] B. Redding, M. Alam, M. Seifert, H. Cao, *Optica* **2014**, *1*, 175.
[23] Z. Wang, S. Yi, A. Chen, M. Zhou, T. S. Luk, A. James, J. Nogan, W. Ross, G. Joe, A. Shahsafi, K. X. Wang, M. A. Kats, Z. Yu, *Nat. Commun.* **2019**, *10*, 1020.
[24] J. Bao, M. G. Bawendi, *Nature* **2015**, *523*, 67.
[25] J. Meng, J. J. Cadusch, K. B. Crozier, *Nano Lett.* **2020**, *20*, 320.
[26] W. Hartmann, P. Varytis, H. Gehring, N. Walter, F. Beutel, K. Busch, W. Pernice, *Nano Lett.* **2020**, *20*, 2625.
[27] S. Yuan, D. Naveh, K. Watanabe, T. Taniguchi, F. Xia, *Nat. Photonics* **2021**, *15*, 601.
[28] A. Li, Y. Fainman, *Nat. Commun.* **2021**, *12*, 2704.
[29] J. Zhang, Z. Cheng, J. Dong, X. Zhang, *Optica* **2022**, *9*, 517.
[30] J. Xiong, X. Cai, K. Cui, Y. Huang, J. Yang, H. Zhu, W. Li, B. Hong, S. Rao, Z. Zheng, S. Xu, Y. He, F. Liu, X. Feng, W. Zhang, *Optica* **2022**, *9*, 461.
[31] X. Chen, X. Gan, Y. Zhu, J. Zhang, *Nanophotonics* **2023**, *12*, 715.
[32] H. Xu, Y. Qin, G. Hu, H. K. Tsang, *Light: Sci. Appl.* **2023**, *12*, 64.
[33] Z. Lin, S. Yu, Y. Chen, W. Cai, B. Lin, J. Song, M. Mitchell, M. Hammood, J. Jhoja, N. A. F. Jaeger, W. Shi, L. Chrostowski, *Optica* **2023**, *10*, 497.
[34] M. Piels, D. Zibar, *Sci. Rep.* **2017**, *7*, 43454.
[35] H. Cao, *J. Opt.* **2017**, *19*, 060402.
[36] L. Gao, Y. Qu, L. Wang, Z. Yu, *Nanophotonics* **2022**, *11*, 2507.
[37] R. G. Baraniuk, *IEEE Signal Process. Mag.* **2007**, *24*, 118.
[38] C.-C. Chang, H.-N. Lee, *Opt. Express* **2008**, *16*, 1056.
[39] B. Cerjan, N. J. Halas, *ACS Photonics* **2018**, *6*, 79.

© 2023 Wiley-VCH GmbH

18638899, 0, Downloaded from https://onlinelibrary.wiley.com/doi/10.1002/lpor.202300291 by Westlake University, Wiley Online Library on [23/08/2023]. See the Terms and Conditions (https://onlinelibrary.wiley.com/terms-and-conditions) on Wiley Online Library for rules of use; OA articles are governed by the applicable Creative Commons License

[40] W. Bogaerts, P. De Heyn, T. Van Vaerenbergh, K. De Vos, S. Kumar Selvaraja, T. Claes, P. Dumon, P. Bienstman, D. Van Thourhout, R. Baets, *Laser Photonics Rev.* **2012**, *6*, 47.
[41] Z. Yang, T. Albrow-Owen, H. Cui, J. Alexander-Webber, F. Gu, X. Wang, T.-C. Wu, M. Zhuge, C. Williams, P. Wang, A. V. Zayats, W. Cai, L. Dai, S. Hofmann, M. Overend, L. Tong, Q. Yang, Z. Sun, T. Hasan, *Science* **2019**, *365*, 1017.
[42] P. Wang, R. Menon, *Opt. Express* **2014**, *22*, 21541.
[43] H. Xu, Y. Qin, G. Hu, H. K. Tsang, *ACS Photonics* **2023**, *10*, 654.
[44] Z. Cheng, Y. Zhao, J. Zhang, H. Zhou, D. Gao, J. Dong, X. Zhang, *ACS Photonics* **2021**, *9*, 74.
[45] M. Corato-Zanarella, A. Gil-Molina, X. Ji, M. C. Shin, A. Mohanty, M. Lipson, *Nat. Photonics* **2022**, *17*, 157.

© 2023 Wiley-VCH GmbH

18638899, 0, Downloaded from https://onlinelibrary.wiley.com/doi/10.1002/lpor.202300291 by Westlake University, Wiley Online Library on [23/08/2023]. See the Terms and Conditions (https://onlinelibrary.wiley.com/terms-and-conditions) on Wiley Online Library for rules of use; OA articles are governed by the applicable Creative Commons License